ASME Journal of Turbomachinery
Online journal at:
https://asmedigitalcollection.asme.org/turbomachinery

# Time-Averaged Aerodynamics of a High-Speed Low-Pressure Turbine Cascade With Cavity Purge and Unsteady Wakes

**G. Lopes**[1]
Turbomachinery and Propulsion Department,
von Karman Institute for Fluid Dynamics,
Rhode Saint Genèse 1640, Belgium
e-mail: gustavo.lopes@vki.ac.be

**L. Simonassi**[2]
Turbomachinery and Propulsion Department,
von Karman Institute for Fluid Dynamics,
Rhode Saint Genèse 1640, Belgium
e-mail: loris.simonassi@avioaero.it

**S. Lavagnoli**
Turbomachinery and Propulsion Department,
von Karman Institute for Fluid Dynamics,
Rhode Saint Genèse 1640, Belgium
e-mail: lavagnoli@vki.ac.be

*The time-averaged aerodynamics of a high-speed low-pressure turbine (LPT) cascade were investigated under the impact of unsteady wakes and purge flows. The tests were performed at an outlet Mach (M) and Reynolds numbers (Re) of 0.90 and 70 k, respectively. Unsteady wakes were simulated by means of a spoked-wheel type wake generator (WG), and a reduced frequency of 0.95 was achieved. The development of a purge flow system to operate at low-pressure levels is presented alongside guidelines for the operation of the circuit. The new purge system was commissioned in terms of its long-term stability and flow uniformity at the cascade inlet. The impact of varying purge flows from a cavity versus a flat endwall was assessed by means of static pressure measurements on the blade pressure side (PS) and suction side (SS) and traverses performed downstream with a miniaturized multi-hole probe. Differences in the secondary flow structures resultant from injecting purge flow into the flowfield are observed, namely, the intensification of the trailing shed vortex (TSV) and passage vortex (PV) that is also displaced away from the endwall. An increase of the endwall losses occurs as the flat endwall was replaced with a cavity geometry and the cavity purge flowrate increases.*
[DOI: 10.1115/1.4063878]

*Keywords: cavity and leaking flows, impact on cavity leaking flows on performance*

## 1 Introduction

The ultra-high by-pass ratio geared turbofan (GTF) enables a reduction of the specific fuel consumption, low-pressure turbine (LPT) stage count, and weight [1] comparatively to modern turbofans. The latter can account for as much as one-thi rd of the overall engine weight [2]. Torre et al. [3] performed a thorough investigation of a high-speed LPT in a transonic rotating rig. Their work also highlights the difference in the operating conditions between conventional and high-speed LPTs. Due to the increase in rotational velocity of the low-pressure spool imposed by the gearbox, the LPT operates at transonic exit Mach numbers ($M_{out} > 0.80$) in combination with low Reynolds numbers encountered during cruising regime [4]. The combination of these flow regimes has been highlighted as one of the main challenges in the development of transonic LPTs for GTFs [5,6].

The development of secondary flows in axial turbines is a relatively well-understood matter due to several models developed under steady flow conditions [7–10]. However, the flow in axial turbines is dominated by unsteady complex interactions between blade rows [11]. Linear cascade testing is an attractive testing environment in the sense that different flow phenomena and geometrical features can be varied parametrically to decouple flow effects. The experimental setups are often easier to implement in a computational fluid dynamics (CFD) setup or to complement existing analytical models that rely on linear cascade data.

In a linear cascade environment, the interactions between blade rows have been addressed in experiments where unsteady wakes have been recreated by means of moving bars [12–15]. Experiments in linear cascades allow to match the engine-relevant Reynolds number (nondimensional parameter dominating performance in LPT blading), Mach number (relevant in high-pressure turbine (HPT) blading), and/or velocity triangles. However, literature where the three parameters coexist during the experiments is scarce.

The complexity of the flowfield present in axial turbines is further aggravated by the purge flows emerging from the turbine rim seal that contribute to the losses due the mixing with the annulus main flow [16] and alter the inlet flow to the upcoming blade row as well as the structure of the endwall flows in the passage. In general terms, investigations performed in turbines report increasing losses and intensification of the endwall flow structures with the increasing purge flowrate [17–26].

Barigozzi et al. [27] experimentally investigated the impact of the purge flowrate and gap geometry on the aerothermal performance of an HPT rotor blade in a linear cascade configuration. The purge flow injection angle was achieved by means of fins installed in the gap. They found increasing mixed-out losses and film cooling

[1]Corresponding author.
[2]Present address: Avio Aero, 10040 Rivalta di Torino TO, Italy.
Manuscript received August 9, 2023; final manuscript received September 6, 2023; published online November 13, 2023. Tech. Editor: David G. Bogard.

effectiveness with the increasing purge flowrate. The latter was attributed to the intensification of the pressure side (PS) leg of the horseshoe vortex that develops into the passage vortex (PV). They also highlighted the importance of the coolant injection angle that aims at retrieving the stator–rotor platform relative motion in the real machine in the linear cascade setup. Neglecting the tangential velocity in their linear cascade led to an underestimation of the secondary flow losses. de la Rosa Blanco et al. [28] experimentally investigated the impact of the gap geometry (backward and forward facing steps), tangential velocity and purge flowrate on the performance of a modern LPT blade operating with a PS separation bubble in a linear cascade setup under steady flow conditions and relevant Reynolds number (232,000). The investigation is complemented by numerical results. The study reports an increase of the losses with the increasing purge flow, while being dependent on the gap geometry. The latter determines the extent with which the purge flow interacts with the PS separation bubble. Similar to the study of Barigozzi et al. [27], the tangential velocity component was found to be relevant to the development of the endwall flows. In addition, it was found that the endwall flows and mixed-out losses in the presence of the gap geometry when no purge flow is being injected are impacted due to the exchange of mass and momentum between the fluid that recirculates in the gap geometry and the main flow.

The latter investigation was complemented in the work performed by Popovic and Hodson [29]. A parametric investigation around the interaction of the purge flow emerging from an overlapping rim-seal geometry and the main flow was performed numerically in a linear cascade setup. Similar to the findings reported in Ref. [28], the backward facing step was found to be detrimental to the losses. The study also reports that shifting the gap closer to the blade leading edge (LE) promoted a reduction of the effects of the negative relative tangential velocity of the purge flow. The latter effects resulted from having the mixing of the purge flow and mainstream within the outer part of the rim seal. On the other hand, shifting the gap away from the LE promoted a more uniform flow field at the outlet of the rim seal at the cost of the increased cross-passage flow and higher losses.

Due to the impact of the gap geometry on the secondary flow strength and losses even when no purge flow is injected, some works have highlighted the significance of including the endwall gap geometry in the early design stages of turbines [17,30]. Even though including a detailed geometry can be prohibitive in the early design phase, MacIsaac et al. [31] has shown that a simplified geometry should be used nonetheless, being especially attractive for optimization schemes.

The previous studies, performed in a linear cascade environment, lack the inclusion of unsteady wakes that interact with the purge flows and impact the secondary flow development and losses. Open literature dealing with experimental investigations performed in a linear cascade environment in the presence of purge flows at engine-relevant Mach, Reynolds, and unsteady wake reduced frequency is not available at this moment in time.

This research develops on recent investigations performed in the scope of the EU project SPLEEN, which aims to extensively characterize the interaction of purge flows with endwall flows in high-speed LPTs. Recently, Lopes et al. [32] characterized the steady aerodynamics of an open access transonic LPT geometry tested at its on- and off-design operating point in a linear cascade environment at engine-relevant Mach and Reynolds numbers. The latter work was extended to include unsteady wakes with similar velocity triangles as the ones found in a real-engine environment [33,34]. This work aims at extending the previous works and existing literature on the impact of purge flows on a high-speed LPT under the effects of unsteady wakes. To do so, detailed measurements of the inlet flow field to the cascade are presented upstream and downstream the purge flow slot. The impact of an engine-representative cavity geometry on the blade aerodynamics and downstream flowfield is assessed in the absence of purge flowrate and for two purge flowrates. The blade aerodynamics are characterized by means of pressure measurements performed with a traversable blade. The downstream flowfield deviation and losses are characterized by means of a directional pressure probe. The experimental data described in this article can be obtained at the open access repository [35].

## 2 Experimental Methods

**2.1 SPLEEN Test Case.** A thorough description of the test case can be found in Ref. [36]. The C1 cascade is representative of a rotor hub geometry of a geared LPT. Figure 1 (left) displays the blade geometry along some key characteristics contained in Table 1.

The linear cascade consists of 23 blades with a span ($z$) of 165 mm. This investigation was conducted at the nominal operating point ($M_{out} = 0.90$; $Re_{out} = 70$ k). The freestream turbulence intensity was kept fixed at $\sim 2.40\%$ by means of a passive turbulence grid. The simulation of unsteady wakes was achieved by means of a spoked-wheel type wake generator (WG) mounted with 96 cylindrical bars with 1.00 mm of diameter. The bar diameter was selected to be similar to the trailing edge (TE) thickness to generate wake profiles representative of a thin LPT TE [37]. The bar tip reached $\sim 73\%$ of the cascade span when parallel to the central blade LE. The wake reduced frequency ($f^+$) at the midspan was $\sim$0.95, which resulted in a flow coefficient of $\sim$0.80. A slot between the WG and linear cascade was used to inject purge/leakage flow in the test section with purge mass flow ratios ranging between 0% and 1%. Figure 1 (right) displays the cascade installed in the rig test section. In the latter, the WG bars and cavity slot are highlighted to aid the visualization of the setup.

**2.2 The VKI S-1/C High-Speed Linear Cascade.** The measurements were conducted in the high-speed, low-Reynolds linear cascade S-1/C of the von Karman Institute. A schematic view of the wind tunnel is shown in Fig. 2. The wind tunnel is a continuous closed-loop facility driven by a 615 kW 13 stages axial flow compressor. The flow temperature was kept near ambient by means of an air-to-water heat exchanger.

The mass flow was regulated via the adjustment of the compressor rotational speed and a by-pass valve. A vacuum pump regulated

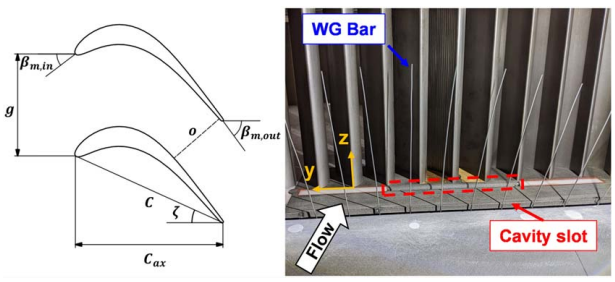


**Fig. 1 SPLEEN C1 cascade blade geometry (left) and test section installed with cascade highlighting main features (right)**

**Table 1 C1 cascade key geometrical features**

| Nom. | Dim. | Units |
|---|---|---|
| Chord, $C$ | 52.280 | mm |
| Axial chord, $C_{ax}$ | 47.614 | mm |
| Pitch, $g$ | 32.950 | mm |
| Cascade span, $z$ | 165.000 | mm |
| Inlet metal angle, $\beta_{met,in}$ | 37.300 | deg |
| Outlet metal angle, $\beta_{met,out}$ | 53.800 | deg |
| Stagger angle, $\zeta$ | 24.400 | deg |

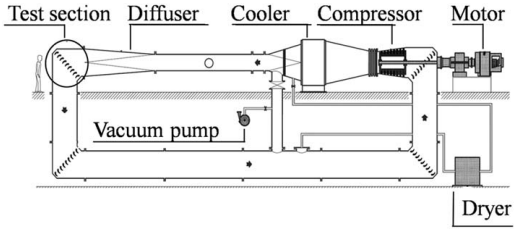


**Fig. 2 The VKI S-1/C wind tunnel**

the pressure level inside the facility, allowing to reach minimum absolute pressure values in the order of 5000 Pa. The cascade test section was mounted in the first elbow of the loop, following the diffuser. Wire meshes and honeycombs upstream of the test section ensured homogeneous inlet flow conditions. The outlet Mach and Reynolds numbers could be set independently. The free-stream turbulence intensity was set by means of a movable passive turbulence grid. More details of the facility can be found in Ref. [36].

### 2.3 Purge Flow Circuit

*2.3.1 Hardware and Instrumentation.* A new purge flow system was developed to inject purge flow at the cascade inlet. The latter consisted of a circuit that made use of the pressure drop between a high-pressure region within the rig (immediately downstream of the compressor) and the purge location near the test section. The circuit connecting both ends is depicted in Fig 3.

Two ball valves (V1 and V3) were used to fine-tune the amount of bypassed flow to be purged upstream of the cascade. The use of two ball valves was selected to ensure that tests can be performed in case that the pipe containing the orifice plate must be accessed for maintenance or calibration of embedded instrumentation. In this case, both valves can be closed to seal the main loop of the VKI S-1/C. An additional gate valve was used to draw air from the atmosphere in case the pressure ratio was not sufficient to accomplish the required massflow rate.

The measurement of the massflow rate was performed by means of an orifice plate mounted inside a PVC pipe with an inner diameter of 53 mm. The orifice had a diameter of 35 mm. To track the massflow rate inside the circuit, a differential pressure sensor (Validyne DP45 with a range of ±550 Pa) was used to measure the pressure drop across the orifice. Additionally, the static pressure upstream of the orifice was measured with reference to the cascade reference pressure (shown later). To that effect, an additional Validyne DP45 with a range of ±3500 Pa was used.

These measurements were complemented with flow temperature measurements performed by a type-K thermocouple near the orifice plate. Downstream of the orifice plate, the flow encountered a splitter that guided the flow through 12 small flexible pipes that were fed into the cavity settling chamber (explained later). Upstream of the splitter, the flow total and static pressures as well as the total temperature were also measured, by means of two Validyne DP45 with a range of ±3500 Pa and referenced to the cascade reference pressure and an additional type-K thermocouple, respectively.

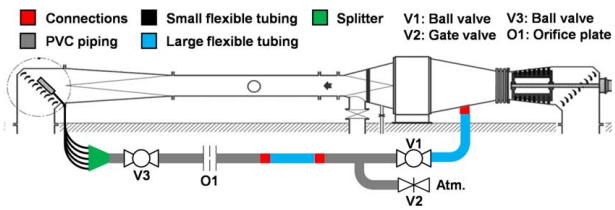


**Fig. 3 Purge flow circuit constituents in relation to the upper loop of VKI S-1/C**

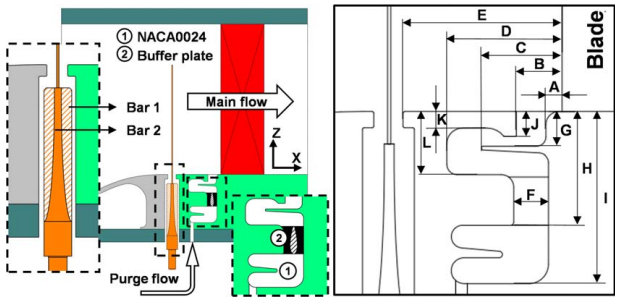


**Fig. 4 View of test section with detail of WG bar support and cavity structural elements: (1) buffer plate and (2) NACA0024 (left) and cavity geometry key dimensions (right)**

*2.3.2 Operating Principle.* The purge flowrate in the rig, $\dot{m}_{\text{rig}}$, setup was scaled to respect the purge massflow ratio (PMFR) encountered in the engine. The PMFR is defined as the ratio of purge massflow to engine core massflow. Based on the engine operating conditions and the aero-thermodynamic properties encountered in a typical test performed in the VKI S-1/C ($T_{0,\text{rig}} = 284.1$ K and $P_{0,\text{rig}} = 8880$ Pa), the $\dot{m}_{\text{rig}}$ that is required to match the engine PMFR was computed. This value corresponded to the design point (DP) and had to be adjusted for day-to-day real-time operations. Since the $T_0$, rig varied during the tests, the $P_0$, rig was also adjusted to keep the outlet Mach and Reynolds numbers matched. This caused a mismatch in the mass flowrate required to match the goal PMFR.

The required mass flowrate to be injected to match the engine point could then be obtained based on the aero-thermodynamic properties during the tests as follows:

$$\dot{m}_{\text{rig,test}} = \dot{m}_{\text{rig,DP}} \frac{\sqrt{T_{0,\text{DP}}/T_{0,\text{test}}}}{P_{0,\text{DP}}/P_{0,\text{test}}} \tag{1}$$

where $T_0$, DP and $P_0$, DP are the total temperature and pressure, respectively, used in the scaling from the engine configuration and $T_0$, test and $P_0$, test are the total temperature and pressure, respectively, during any test performed in the VKI S-1/C.

The purge flowrate was computed based on the standard ASME MFC-3M-2004 [38], which depends on the orifice plate and connecting pipe geometries:

$$\dot{m}_{\text{rig,test}} = C_d \epsilon \frac{\pi d^2}{4} \sqrt{\frac{2\rho_{\text{in}} \Delta P}{1-\beta^4}} \tag{2}$$

where $C_d$ is the discharge coefficient, $\epsilon$ is the expansibility factor, $d$ is the orifice diameter, $\rho_{\text{in}}$ is the density upstream of the orifice (computed with the fixed instrumentation described previously), $\Delta P$ is the pressure drop across the orifice, and $\beta$ is the ratio of inner to outer diameter. The computation of $C_d$ and $\epsilon$ are described in Ref. [38]. During the test, the valves in the purge flow circuit were adjusted so that the $\dot{m}_{\text{rig,test}}$ computed with Eq. (2) matched the required one computed with Eq. (1).

*2.3.3 Cavity Geometry.* An engine-representative cavity geometry was used. The cavity was placed between the WG slot and the cascade. Figure 4 (left) highlights the relative position between the WG bar, cavity, and blade in a meridional view of the cascade test section. The splitter fed the cavity settling chamber through 12 equidistant pipes to reduce flow nonuniformities as the flow developed within the cavity. In addition, a buffer plate (element 1 in Fig. 4, left) was introduced to increase mixing and homogenize the flow in the cavity. A CFD investigation on the impact on the buffer plate was performed (not presented here). It was found that a maximum variation in the nondimensional total pressure at the cavity outlet can be reduced by a factor of two compared to a case where no buffer plate is used.

**Table 2 Key dimensions of cavity geometry**

| Nom. | Units | Nom. | Units |
|---|---|---|---|
| A | 0.1329 $C_{ax}$ | G | 0.2850 $C_{ax}$ |
| B | 0.3754 $C_{ax}$ | H | 0.9302 $C_{ax}$ |
| C | 0.6604 $C_{ax}$ | I | 1.4088 $C_{ax}$ |
| D | 0.9454 $C_{ax}$ | J | 0.2042 $C_{ax}$ |
| E | 1.3046 $C_{ax}$ | K | 0.1361 $C_{ax}$ |
| F | 0.2850 $C_{ax}$ | L | 0.5147 $C_{ax}$ |

**Table 3 Summary of investigated cases**

| Nom. | Endwall | Bar | PMFR |
|---|---|---|---|
| NC | Flat | 1 | 0.00% |
| C: PMFR=0.00% | Cavity | 2 | 0.00% |
| C: PMFR=0.50% | Cavity | 2 | 0.50% |
| C: PMFR=0.90% | Cavity | 2 | 0.90% |

To avoid spoiling the purge outlet flow, no swirler was mounted near the cavity outlet. The only available location for a possible swirler was where a structural element was placed (element 2 in Fig. 4, left). A CFD study was conducted to compare the cascade outlet flow field for the cases where a swirler with 45 deg turning versus the case where a symmetrical profile (NACA0024) was used. It was found that the cavity geometry downstream of the structural elements dampened the tangential velocity component imposed by the swirler. For this reason, the symmetrical element was used in this study. An underprediction of the secondary losses comparatively to a linear cascade setup with the swirled purge flow is expected due to the lack of the tangential momentum [27,28,39]. A detailed view of the cavity geometry with key dimensional parameters is displayed in Fig. 4 (right). The dimensions are reported in Table 2 for completeness.

**2.4 Flow Conditions.** The setups used in this work are combinations of the cavity endwall and the WG bar support. For all the setups, the cascade outlet flow conditions and wake reduced frequency correspond to the design point and are the same as investigated in Ref. [33].

Tests were performed with a flat endwall and with the cavity endwall. In the presence of the cavity geometry, three cases are investigated: one case without purge flow and two with increasing $\dot{m}_{rig,test}$. The massflow was adjusted during the test to achieve PMFR = 0.50% and 0.90%. The latter PMFR values result in a blowing ratio of ~0.0614 and ~0.1105, respectively.

Preliminary tests were performed with the cavity slot closed (flat endwall) and with a cylindrical WG bar support that occupied as much of the WG slot as possible to reduce ingress/egress from the slot. However, a mechanical failure of one of the supports led to the redesign of the latter by removing excess material. The resulting support is displayed in Fig. 4 (left) where one can see the elliptical support (bar 2, full orange) as well as the cylindrical one (bar 1, dashed orange surface). The elliptical support was used in the tests performed with the cavity. Table 3 summarizes the investigated cases in terms of the variable parameters. The tests were conducted for a fixed $M_6$, is = 0.90, $Re_6$, is = 70 k, and $f^+ = 0.95$.

**2.5 Experimental Methodology**

*2.5.1 Instrumentation.* The characteristics of the instrumentation were reported with detail by Simonassi et al. [36]. Figure 5 (left) shows the meridional view of the test section, the measurement planes, and the cascade reference system. The pitchwise coordinate ($y$) increases toward passages out of the figure plane. The pitchwise coordinate is zero in the intersection of the plane originating from the blade LE, and following the cascade inlet metal angle, with the plane at which measurements are being performed. A similar logic applies downstream with the TE and outlet metal angle.

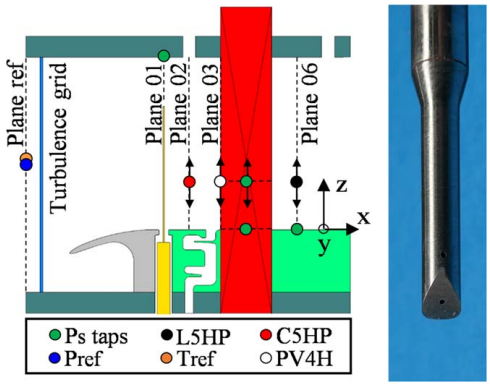


**Fig. 5 Test section layout and instrumentation at each measurement plane (left) and head of pneumatic virtual four-hole cylindrical probe (right)**

The operating point was defined in terms of outlet isentropic Reynolds and Mach number. These were monitored by means of the total pressure and temperature upstream and static pressure downstream of the cascade. The cascade total temperature was measured by means of a type-K thermocouple at "Plane Ref." This plane sat sufficiently far upstream so that reference instrumentation was not impacted by the cascade potential flow field. The work produced by the WG bars was neglected, and therefore, it was assumed that the total temperature across the cascade was conserved. The total pressure at plane 01 was computed based on a correlation built to estimate the total pressure loss across the turbulence grid (TG) and WG at different operating points. The static pressure at the outlet was measured by means of static pressure taps on the lower endwall at plane 06. The taps were connected to a Scanivalve MPS4264–1 PSI.

The inlet flow field of total pressure and incidence were mapped by means of a pneumatic Cobra five-hole probe (C5HP) traversed at plane 02 ($0.50C_{ax}$ upstream of LE). The probe ports were connected to a Scanivalve MPS4264–1 PSI, and aerodynamic calibration coefficients were used to determine the local total and static pressures, as well as yaw and pitch angles in the probe head reference system. The flow angles in the probe reference system were transformed into flow angles in the cascade reference system to compute the incidence ($i$).

A pneumatic virtual four-hole cylindrical probe (PV4HP) was also used at the inlet. The head geometry, displayed in Fig. 5 (right), is inspired by a probe reported in Refs. [40,41]. The diameter of the cylindrical portion of which the head is part of is 2.35 mm. The probe was rotated three times around its axis (−30 deg, 0 deg, and 30 deg) to displace the ports and simulate the measurements of a real three-hole probe. The probe was used at plane 03 (between LE) in two slots, one on each side of the central blade, to assess the inlet flow uniformity into to the cascade two central passages in terms of normalized total pressure and flow incidence.

The cascade losses and deviation were obtained through measurements performed with a pneumatic L-shaped five-hole probe (L5HP) at plane 06 ($0.50C_{ax}$ downstream of TE). The measurement chain and data reduction methodology were the same as for the C5HP. The losses are represented by the energy loss coefficient ($\xi$) and the flow deviation from the primary flow direction is computed as the difference between the primary flow direction ($\beta$) at each spanwise location and the one at midspan.

In addition to the flow field measurements, the phase-averaged blade PS and suction side (SS) aerodynamics were investigated

by means of static pressure taps. Both could be displaced in the spanwise direction from the endwall until midspan. The pressure taps were connected to a Scanivalve MPS4264–1 PSI.

*2.5.2 Uncertainty.* The measurement uncertainty is evaluated according to the ASME uncertainty method [42]. The errors have been categorized as "random" for errors that varied during the measurement period and as "systematic" for errors that were invariant during the measurement period. The uncertainty on generic quantities was determined using a Taylor expansion method, assuming small variations of the dependent parameters.

The uncertainties reported in Table 4 show that systematic terms are generally the largest contributors to the overall measurement uncertainty. As a general consideration, the difference between the same measurement performed at different operating points (in terms of cascade operating exit Mach number and Reynolds number), and/or pitch and span locations, is not markedly affected by systematic errors, being the quantities measured by the same calibrated transducers and measurement chains over a relatively unchanged experimental setup [43]. For these reasons, the uncertainty on the comparison of the measurements in this work is dominated by random error terms, with extremely small systematic uncertainty.

## 3 Results and Discussion

**3.1 Stability and Operating Conditions.** The stability of the flow conditions in the absence of WG and purge flow system is reported in Ref. [36]. The stability of the purge flowrate was assessed with the new constituents operating simultaneously: WG and purge flow system.

Figure 6 contains the normalized probability density function (PDF) of the purge flowrate for PMFR = 0.90% obtained by merging the whole dataset for the tests performed with WG and purge flow. The PDF for the purge flow system displays the variations around the nominal PMFR that was set at the beginning of each test. Even though not displayed, the PDF of the WG rotational velocity and the purge flowrate for PMFR = 0.50% also resembles a Gaussian distribution.

Based on the standard deviation of the PDFs, the rpm during the tests was kept within 3300 ± 0.054. The PMFR were kept within 0.50% ± 0.0023% and 0.90% ± 0.0014%.

**3.2 Inlet Flow Characterization at Plane 02.** The profile of the inlet total pressure measured at plane 02 with the C5HP at $y/g = 0.00$ is displayed in Fig. 7(*a*). The values are normalized by the freestream total pressure at plane 01 ($P_{01}$, fs). The profiles are displayed for a single pitchwise location since the topology of the

**Table 4 Random and systematic uncertainty of measured and computed quantities with 95% confidence interval**

| Instr. | Qt. | Unit | $U_{rand}$ | $U_{sys}$ |
|---|---|---|---|---|
| Fixed | $T_{01}$ | $K$ | 0.002 | 0.518 |
| | $T_{0,orif.}$ | K | 0.002 | 0.504 |
| | $P_{ref}$ | Pa | / | 25 |
| | $\Delta P_{orif.}$ | Pa | 0.012 | 2.809 |
| | $P_{in,orif.}$ | Pa | 1.052 | 20.078 |
| PV4HP | $i$ | deg | 0.24 | 0.36 |
| | $P_{03}/P_{01}$, fs | – | 0.001 | 0.005 |
| C5HP | $i$ | deg | 0.24 | 1.11 |
| | $P_{02}/P_{01,fs}$ | – | 0.001 | 0.005 |
| Blade | $M_{is}$ | – | 0.0007 | 0.0054 |
| L5HP | $\beta$-$\beta_{MS}$ | deg | 0.24 | 0.36 |
| | $\xi$ | – | 0.0019 | 0.0095 |
| Purge | $\dot{m}_{rig,\ test}$ | kg/s | 1.82E-04 | 0.0021 |
| | PMFR | % | 0.0017 | 0.0021 |

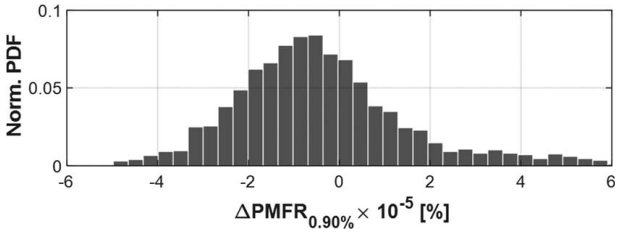


**Fig. 6 Normalized probability density function of purge flowrate when the tests are performed for PMFR = 0.90%**

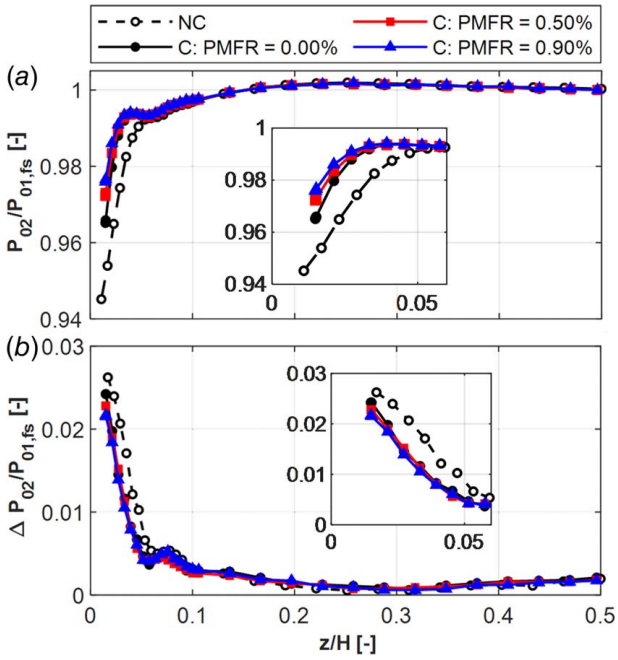


**Fig. 7 Inlet total pressure profiles measured at plane 02 with the C5HP for the investigated endwall geometries at $y/g = 0.00$ (*a*) and maximum pitch-to-pitch variation (*b*)**

profile does not vary in the pitch-to-pitch direction. The maximum pitch-to-pitch variation of the normalized total pressure can be found in Fig. 7(*b*).

The total pressure profiles for the cases with cavity display good agreement. On the other hand, the profiles diverge from the one measured with the flat endwall. Since plane 02 sat upstream of the cavity slot the variation is attributed to the alteration of the bar support, which is likely to have modified the ingress/egress from the WG slot. At $z/H \approx 0.02$, there is a deficit in the measured total pressure as large as 200 Pa, considering an inlet total pressure of 10,000 Pa. On the other hand, the pitch-to-pitch variation along the span is very similar for all the investigated cases. At $z/H = 0.50$, the pressure variation is within ±20 Pa, being within the instrumentation systematic uncertainty. Near the endwall the maximum variation reaches ±125 Pa for the case tested with a flat endwall. The momentum deficit of these profiles is accounted for in the loss breakdown presented later.

The spanwise distribution of incidence at plane 02 is displayed in Fig. 8(*b*) for $y/g = 0.00$ and in the center of the passages adjacent to the central blade (Figs. 8(*a*) and 8(*c*)).

The incidence is computed as follows:

$$i = \beta_{in} - \alpha_{met} \tag{3}$$

For all the investigated cases, the spanwise distribution of incidence is negative throughout the span. The incidence decreases

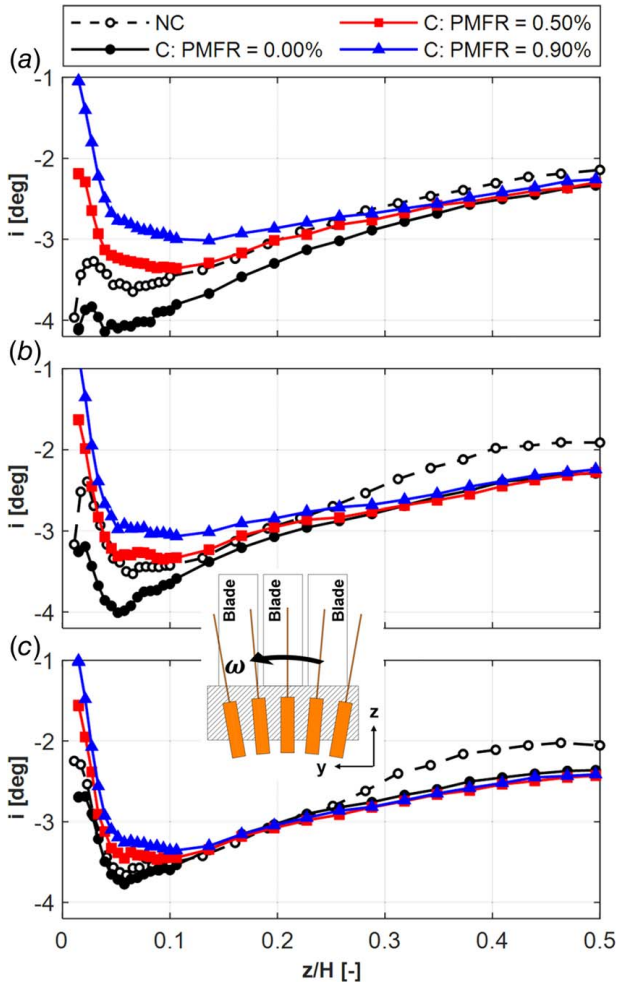


**Fig. 8 Spanwise distribution of incidence measured at plane 02 with the C5HP for the investigated endwall geometries at: (*a*) $y/g = -0.50$, (*b*) $y/g = 0.00$, and (*c*) $y/g = +0.50$**

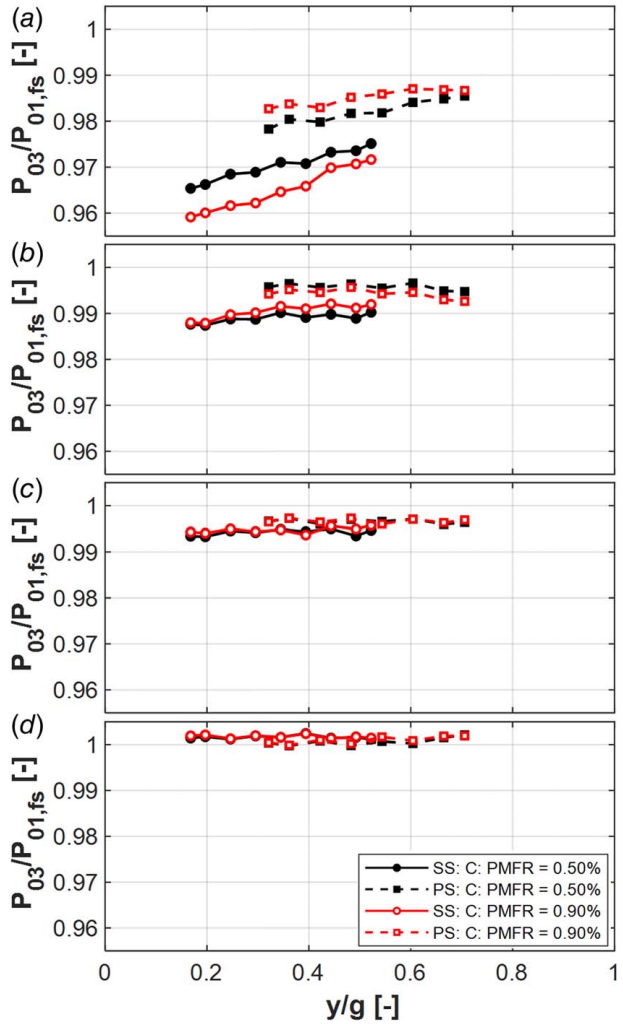


**Fig. 9 Pitchwise distribution of normalized total pressure at plane 03 measured with PV4HP at: (*a*) $z/H = 2.61\%$, (*b*) $z/H = 5.03\%$, (*c*) $z/H = 9.88\%$, and (*d*) $z/H = 46.36\%$**

toward the endwall up to a local minimum depending on the pitchwise location, after which there is a partial recovery of incidence. A maximum pitch-to-pitch variation of ±0.10 deg exists at midspan for all cases. Near the endwall, the latter reaches ±0.50 deg when purge flow is injected, and as much as ±1.50 deg for the cases with flat endwall and cavity endwall without purge flow injection. For a fixed pitchwise location, the variation in the incidence between the investigated cases is larger at $y/g = -0.50$ (see Fig. 8(*a*)), where the variation can reach ±1.50 deg at the location of the point closest to the endwall. The difference between the cases is significantly reduced at $y/g = +0.50$ (see Fig. 8(*c*)). The pitch-to-pitch variations are impacted by the possible WG slot ingress/egress since the bars are dragging/pushing air into the slot because of the rotational motion (see sketch of the WG in Fig. 8).

**3.3 Flow Uniformity at Plane 03.** Figure 9 displays pitchwise distributions of the normalized total pressure measured at plane 03 by means of the PV4HP. The traverses performed on each side of the central blade (one slot near SS of central blade and the other near the PS) are combined by re-shifting them into a normalized pitch.

For both PMFR, a pitch-to-pitch variation in the normalized total pressure is observed. The severity of the nonuniformity is larger near the endwall. At $z/H = 2.61\%$ (see Fig. 9(*a*)) near $y/g = +0.50$, this difference amounts to ∼0.0081 and ∼0.0145 for the cases of PMFR = 0.50% and 0.90%, respectively. For a typical inlet total pressure encountered during testing of 10,000 Pa, the

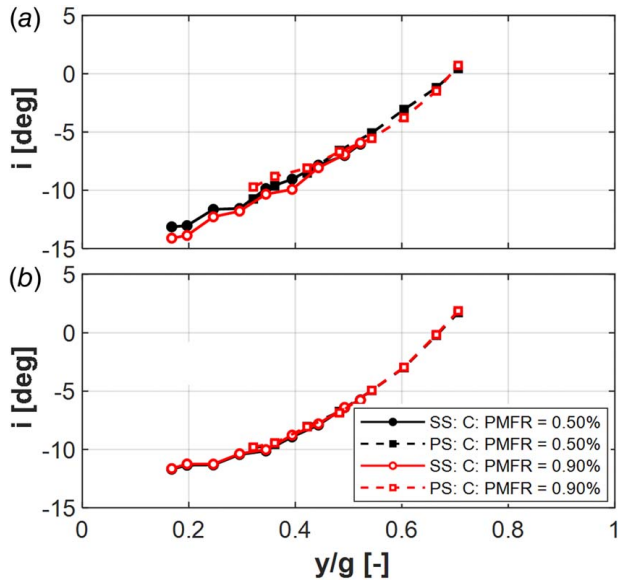


**Fig. 10 Pitchwise distribution of incidence at plane 03 measured with PV4HP at: (*a*) $z/H = 2.61\%$ and (*b*) $z/H = 46.36\%$**

latter values translate into a pressure difference of ~81 Pa and ~165 Pa, respectively. The difference is greatly attenuated as the distance to the endwall increases. At $z/H = 5.03\%$ (see Fig. 9(*b*)), the difference is larger for the lowest PMFR investigated and remains similar to the previous spanwise location (~75 Pa). On the other hand, the difference for the highest PMFR is reduced to ~45 Pa.

The difference between the normalized pressure keeps decreasing up to $z/H = 9.88\%$ (see Fig. 9(*c*)), where the pitch-to-pitch variations of the whole spanwise distribution are within ±16 Pa, highlighting the "start" of the two-dimensional flow region at the inlet. Until close to midspan (see Fig. 9(*d*)), the difference is further reduced, and the pitch-to-pitch variation is within ±10 Pa.

Opposite to the normalized total pressure profiles, the incidence measured with the probe is independent of the spanwise location. Figure 10 displays the pitchwise distribution of the incidence at (*a*) $z/H = 2.61\%$ and (*b*) $z/H = 46.36\%$. The incidence varies nearly linearly between the two reported spanwise locations for each normalized pitchwise location. The distributions display very good pitch-to-pitch uniformity, and the profiles are continuous throughout the normalized pitch. The main variation in incidence occurs for the lowest pitchwise location (near blade PS) where the incidence varies by ~2.5 deg.

**3.4 Blade Aerodynamics.** Figure 11 displays the difference in the isentropic Mach number distributions computed with the static pressure taps and freestream total pressure between the case with a flat endwall and the cases with cavity. The quantities are plotted along the surface position ($s$) along the surface length ($S_L$) of the blade pressure and the suction side. The contours are displayed from the endwall to $z/H = 0.20$, at which the flow is two dimensional. A subtle difference in the loading is observed for the case where the cavity is present, but no purge flow is injected (see Fig. 10(*a*)). The difference at $z/H = 0.20$ is justified by the fact that the outlet Mach number achieved for the case without endwall is slightly higher (≈0.906 versus 0.900). The same feature can be observed for the cases of PMFR = 0.50% and 0.90% in Figs. 11(*b*) and 11(*c*), respectively.

The difference in the isentropic Mach number between the cases with flat endwall and the cavity endwall without purge flow (see Fig. 11(*a*)) is the largest near the LE on the SS because of the different incidence reported previously. This is further aggravated for the cases with purge flow where a large reduction of the isentropic Mach number on the SS occurs because of the impingement of the purge flows. The variations of the blade isentropic Mach number can be better visualized in the plot containing the distributions for all the cases at $z/H = 1.52\%$ (see Fig. 12(*a*)).

The regions on the blade SS dominated by the secondary flow structures ($s/S_L > 0.30$) are greatly modified in the presence of purge flow injection. Near the endwall ($z/H = 1.52\%$), the isentropic Mach number is reduced by as much as 0.080 and 0.084 for the cases of PMFR = 0.50% and 0.90% at $s/S_L \approx 0.40$, respectively (see Fig. 12(*a*) with individual blade distributions). These variations occur in the region where the SS corner vortex is expected.

At $z/H \approx 2.50\%$, the isentropic Mach number is comparable between all cases. After this location, the isentropic Mach number for the cases without purge flow becomes lower than the cases with purge flow injection (see Fig. 12(*b*)). The isentropic Mach number at $z/H = 5.15\%$ for the case of PMFR = 0.50% and 0.90% is higher than the case with the flat endwall by 0.027 and 0.036, respectively. The region where the isentropic Mach number is higher for the cases with purge flow ends at $z/H = 10.00\%$. As it will be displayed later, the passage vortex is

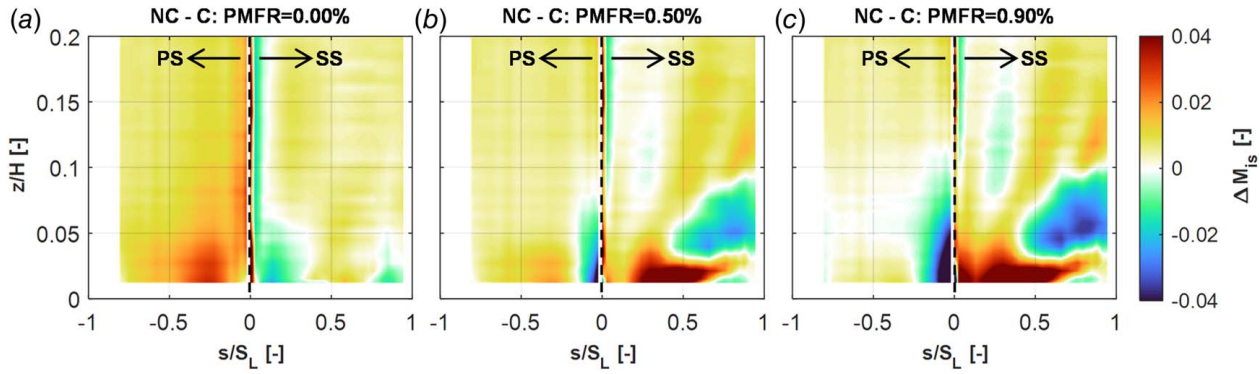


**Fig. 11 Variation in the isentropic Mach number computed on the blade PS and SS surfaces. The PS is represented in the negative coordinate. The variation is computed between the cases with cavity and purge flowrate of: (*a*) 0.00%, (*b*) 0.50%, and (*c*) 0.90% and the case without cavity.**

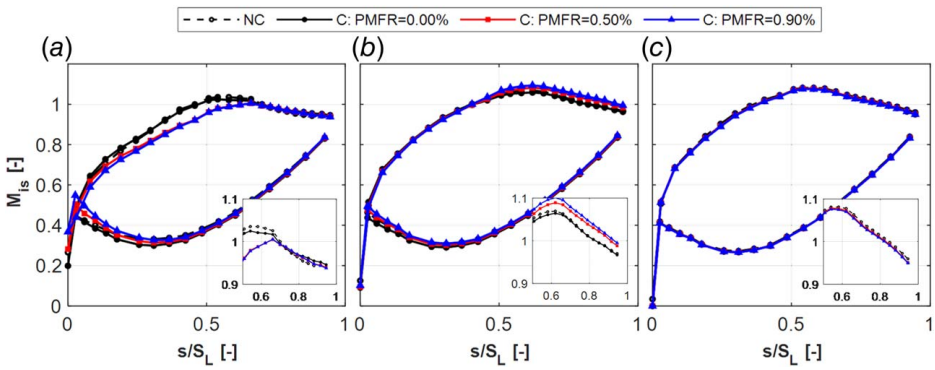


**Fig. 12 Blade isentropic Mach number for all cases investigated at: (*a*) $z/H = 1.52\%$, (*b*) $z/H = 5.15\%$, and (c) $z/H = 50.00\%$**

constrained in a region with similar spanwise extent. After $z/H = 20.00\%$, there is little spanwise variation of the isentropic Mach number. The distributions at midspan (see Fig. 12(*c*)) are in good agreement and suggest that the extent of the impact that the purge flows have on the blade loading is constrained near the endwall.

### 3.5 Outlet Flow Field

*3.5.1 Energy Loss Coefficient.* Contours containing the spanwise and pitchwise distribution of the energy loss coefficient are displayed in Figs. 13(*a*)–13(*d*).

The latter is defined as follows [44]:

$$\xi = 1 - \frac{1 - \left(\frac{P_6}{P_{06}}\right)^{\frac{\gamma-1}{\gamma}}}{1 - \left(\frac{P_6}{P_{01,fs}}\right)^{\frac{\gamma-1}{\gamma}}} \tag{4}$$

The freestream total pressure at the inlet is used. For all cases, a similar topology is observed: a core of higher loss exists at $z/H \approx 0.10$ (core 1). This loss core is mainly impacted by the trailing shed vortex (TSV). For the cases with cavity, an additional loss core near the endwall occurs in the region where the SS corner vortex is typically found (core 2).

The introduction of the cavity impacts the secondary flow development as reported in the works of Refs. [28,29,31]. Mass and momentum exchange between fluid that recirculates in the slot and the mainstream occurs, mainly in regions of the slot where the static pressure distribution upstream of the LE is lower. Typically, the cavity leakage vortex interacts with the pressure side leg of the horseshoe vortex, giving rise to a stronger passage vortex. Comparing Figs. 13(*a*) and 13(*b*), one can see that the loss magnitude and location of core 1 does not change significantly (reduction of loss coefficient below 1%) with the introduction of the cavity endwall. On the other hand, the extent of the region associated with the SS corner vortex enlarged even though the loss magnitude did not increase significantly. The injection of purge flow does not modify the SS corner vortex region significantly nor the magnitude of core 2. However, the magnitude of core 1 increases by 11% and 17% compared to the case with cavity and without purge injection for the cases with PMFR = 0.50% and 0.90%, respectively. The increase in the purge flowrate also shifts core 2

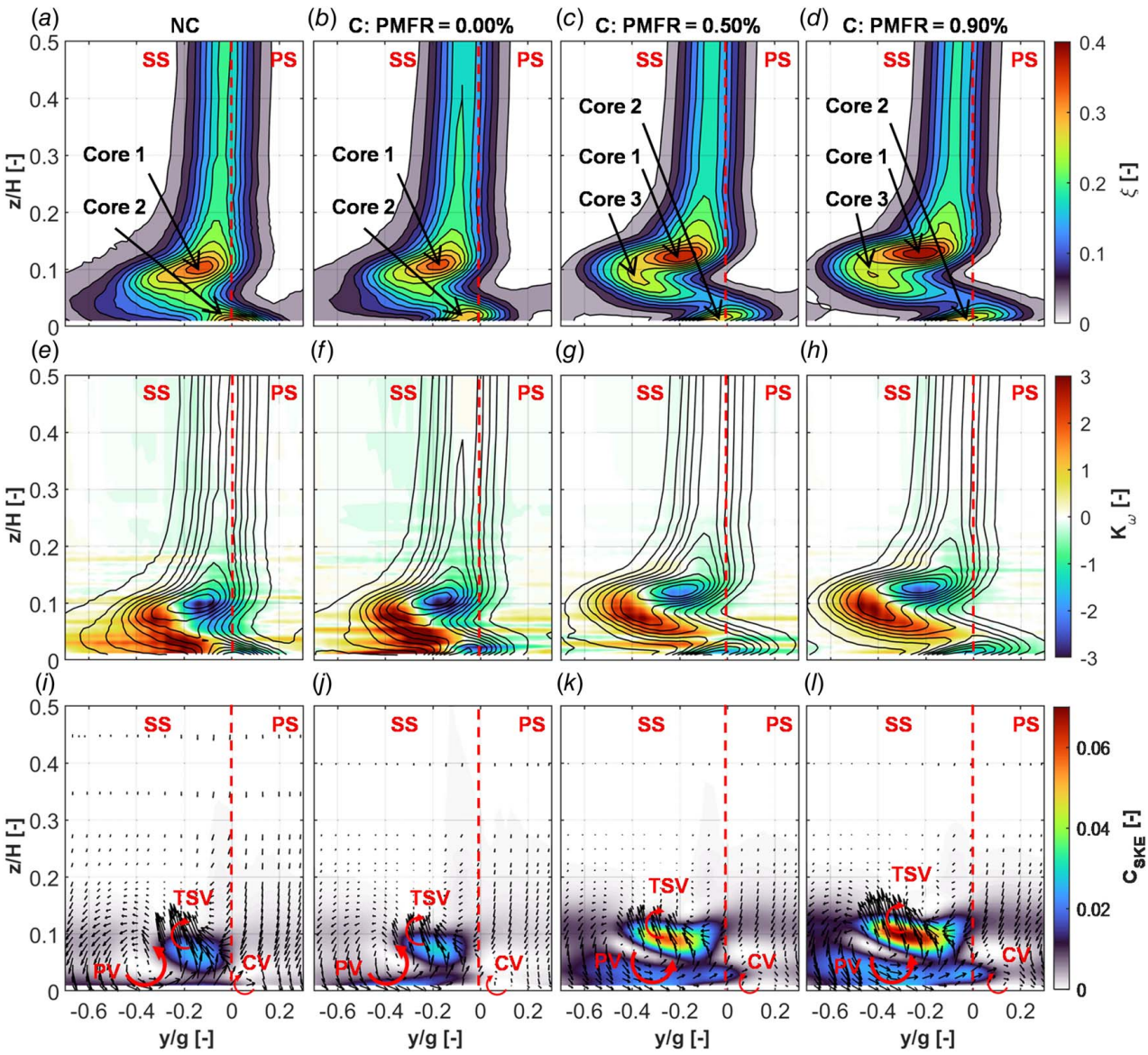


**Fig. 13 (*a–d*) Contours of kinetic energy loss coefficient, (*e–h*) streamwise vorticity coefficient superimposed with energy loss coefficient isolines, and (*i–l*) secondary kinetic energy coefficient superimposed with secondary velocity vectors for the case with flat endwall, with cavity and no purge flow and with cavity with purge flowrate of 0.50% and 0.90%. Observer looks upstream.**

away from the endwall because of the translation of the TSV and PV away from the endwall.

For the cases of PMFR = 0.50% and 0.90%, a new loss core is identified (core 3). The occurrence of this loss peak is due to the larger extent of the PV in the passage. This will be better shown by means of the contours of streamwise vorticity coefficient and pitchwise mass-averaged distributions.

*3.5.2 Streamwise Vorticity Coefficient.* The contours of streamwise vorticity coefficient, $K_\omega$, superimposed with the kinetic energy loss coefficient isolines are displayed in Figs. 13(*e*)–13(*h*). The streamwise vorticity coefficient is computed according to Gregory-Smith et al. [45]:

$$K_\omega = \frac{C}{V_{6,is}}\left(\omega_{ax}\cos\beta_{MS} + \omega_{tan}\sin\beta_{MS}\right) \tag{5}$$

The axial and tangential vorticity components are approximated by:

$$\omega_{ax} = \frac{\partial V_{rad}}{\partial y} - \frac{\partial V_{tan}}{\partial z} \tag{6}$$

$$\omega_{tan} = \frac{1}{V_{ax}}\left(V_{tan}\omega_{ax} + \frac{a^2}{\gamma}\frac{\partial(\ln P_{06})}{\partial z}\right) \tag{7}$$

For all the cases, the PV rotates counterclockwise (observer looking upstream) in the orange colored region. The TSV with clockwise rotation can be identified by the blue region at $z/H \approx 0.10$. Even though limited by the spatial resolution of the L5HP, the SS corner vortex is distinguished by its clockwise rotation located near the endwall.

The streamwise vorticity coefficient in the PV region increases when the cavity endwall is added even in the absence of purge flow. On the other hand, the TSV remains nearly unaltered. When purge flow is injected, the extent of the PV region increases compared to the cases without purge flow. The magnitude of the $K_\omega$ associated with the PV decreases. The same occurs with $K_\omega$ linked to the TSV. Both structures are displaced away from the endwall.

*3.5.3 Secondary Kinetic Energy.* The contours of the secondary kinetic energy coefficient ($C_{SKE}$) for the investigated cases are displayed in Figs. 13(*i*)–13(*l*). The secondary velocity vectors are superimposed to the contours to highlight the secondary flow structures present downstream. The $C_{SKE}$ is defined as follows:

$$C_{SKE} = \frac{\rho_6\left(v_{y,sec}^2 + v_{z,sec}^2\right)}{\gamma P_6 M_{6,is}^2} \tag{8}$$

Where the secondary velocity components, $v_y$, sec and $v_z$, sec, are computed locally on a plane normal to the local primary flow direction. The $C_{SKE}$ provides a good indication of regions of shear between rotating flow structures with surfaces or other structures. In addition, schematic arrows of the structures highlighted in the previous section are added. The dissipation of $C_{SKE}$ is a major contributor to the secondary losses in turbine cascades [46–48]. As it will be presented in the loss breakdown,the endwall loss and $C_{SKE}$ react similarly to the change of endwall and increase of PMFR.

The case without cavity endwall displays a region of increased level of $C_{SKE}$ resultant from the interaction between the PV and TSV. This is practically unaltered as the cavity endwall is inserted, but no purge flow is injected. However, the extent of a region near the endwall increases. MacIsaac et al. [31] found similar features and attributed them to the flow overturning near the endwall region due to the cross-passage pressure gradient.

When purge flow is injected, the $C_{SKE}$ increases because of the interaction of the PV with the TSV. This region is shifted away from the endwall. Comparatively to the case where the cavity endwall is mounted, but no purge flow is injected, an increase in the maximum $C_{SKE}$ by 102% and 148% occur for the cases of PMFR = 0.50% and 0.90%, respectively. This is supported by the increase in the magnitude of the secondary velocities with PMFR.

In addition, the extent of a region near the endwall is also greatly impacted when purge flow was injected. The region extends to the location of the SS corner vortex that also contributes to the $C_{SKE}$ due to the shear interaction with the passage vortex. The pitchwise averaged flow deviation (shown after) displays a higher level of overturning due to the passage crossflow. The latter can also be a justification for the increase in the extent of the near wall region [31].

*3.5.4 Pitchwise Averaged.* The mass-averaged deviation from the primary flow direction, $\beta - \beta_{MS}$, is used to describe the underturning/overturning at the cascade outlet (see Fig. 14(*a*)). The

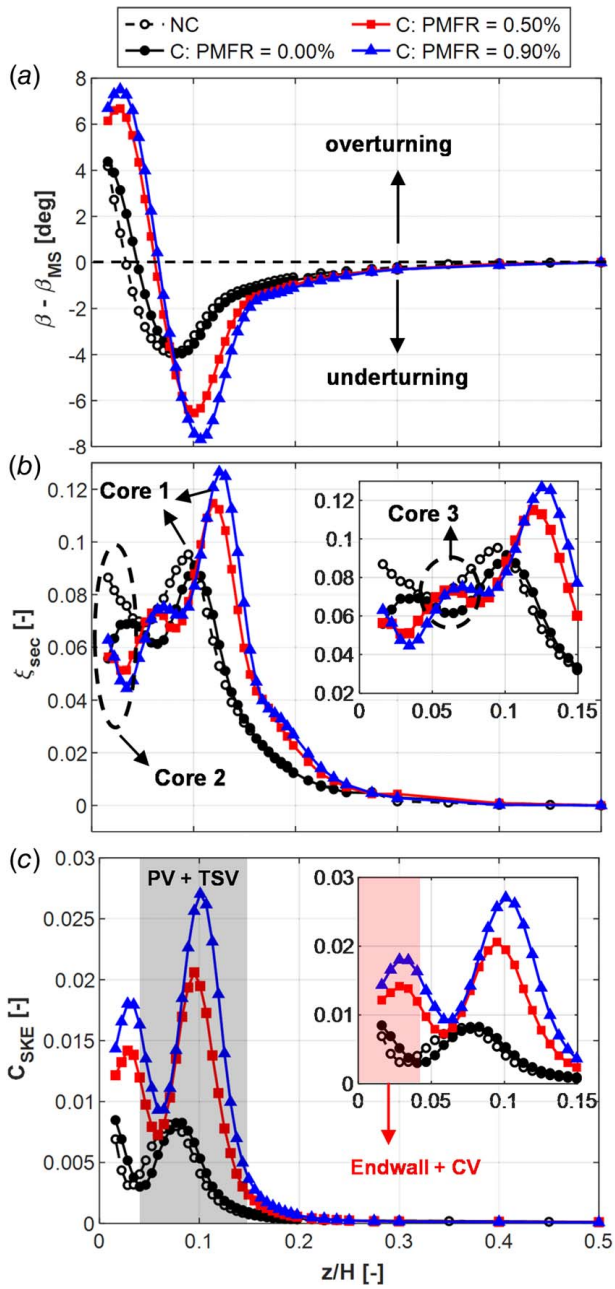


**Fig. 14 Spanwise distribution of: (*a*) mass-averaged primary flow direction, (*b*) secondary kinetic energy loss coefficient, and (c) and secondary kinetic energy**

spanwise distribution of the flow (see Fig. 14(*a*)) displays a region of overturning near the endwall that is mainly impacted by the PV. Further away, the underturning resultant from the interaction of the PV and TSV results in a peak in underturning that is dampened as the span increases.

The difference in the streamwise vorticity coefficient in the TSV region between the case with a flat endwall and the one with cavity endwall without purge flow is practically nonexistent.

This is supported by the similar deviation ranging from midspan to $z/H \approx 0.10$. Introducing the cavity endwall mainly shifts the distribution away from the endwall because of the shift of the PV. When purge flow is injected, the overturning and underturning peaks are doubled. The overturning peak is shifted away from the endwall because of the larger SS corner vortex. In addition, the SS corner vortex intensification promotes a reduction of the overturning caused by the PV near the endwall. Further away from the endwall, the underturning peak is shifted away from the endwall because of the displaced PV and TSV.

To compute the mass-averaged loss (see Fig. 14(*b*)), the total pressure used to compute the energy loss coefficient is mass averaged, while the static pressure is area averaged in the pitchwise direction. Assuming a constant spanwise distribution of the profiles losses [49], the secondary kinetic energy loss coefficient is computed by removing the profile loss from the total energy loss coefficient (see Fig. 14(*b*)). The energy loss coefficient is computed using the inlet freestream total pressure, and therefore, the spanwise distribution includes the contribution of the inlet boundary layer.

Replacing the flat endwall with a cavity slot promotes larger loss content ranging from the endwall to $z/H \approx 0.10$. Even though the magnitude of the losses in core 1 does not increase significantly, the pitchwise extent of the losses is higher for the case with flat endwall, resulting in a peak of higher magnitude and closer to the endwall ($z/H \approx 0.09$ versus 0.10 for case with cavity endwall and no purge) in the spanwise distribution. In addition, the losses near the endwall region ($z/H \approx 0.05$) are higher. The later can be justified by the increased size of the SS corner vortex that consists of lower momentum fluid and has a lower contribution to the pitchwise averaging. The peak associated with the SS corner vortex can still be identified at $z/H \approx 0.03$ for the case with cavity endwall and no purge injection.

The spanwise distribution for the cases with injected purge flow is slightly modified. Near the endwall, a peak of losses is observed. This is due to the balance between the SS corner vortex-induced loss and the region underneath the PV with low losses that does not exist for the cases where the purge flow is not present. This low-loss region is caused by the shift of the PV toward the center of the passage. A decay of the losses occurs up to $z/H \approx 0.03$. The SS corner vortex is contained between the endwall and the valley in the loss profiles. An increase in the losses takes place because of the intensified PV. The peak is displaced away from the endwall with increasing purge flowrate, promoting an increase in the losses of $\sim 3\%$. Even though the loss peak farther away from the endwall is impacted by the PV and TSV, the latter vortical structural is nearer the loss peak in the contour (see Figs. 13(*a*)–13(*d*)).

For the case of PMFR = 0.50%, the maximum loss peak (mainly impacted by TSV) is shifted from $z/H = 0.10$ to 0.12 and its magnitude increases by 27%. When the PMFR is increased to 0.90%, the location of the peak is further displaced to $z/H = 0.13$.

Respectively to the case with cavity endwall and no purge flow, the maximum loss peak is higher by 40%. The larger extent of the TSV toward the center of the passage is observable up to $z/H \approx 0.30$, after which the losses for the cases with and without purge are mainly dominated by the profile loss that is the same.

To complement the previous distributions, the mass-averaged $C_{SKE}$ is shown in Fig. 14(*c*). For all cases investigated, the $C_{SKE}$ produced by the secondary flow structures is constrained between the endwall and $z/H \approx 0.20$ (even though the influence from the TSV on the kinetic energy loss can reach $z/H \approx 0.30$). Starting from the endwall, the combination of the SS corner vortex with the near wall overturning gives rise to a first region of increased $C_{SKE}$ (red shaded region in zoomed image). Toward midspan, there is a decrease of $C_{SKE}$ due to the weak interaction between the secondary flow structures. A following spike above the latter occurs where the PV and TSV interact (black shaded region).

The $C_{SKE}$ distributions for the cases of NC and C: PMFR=0.00% have the same topology along the whole span. Near the endwall, the $C_{SKE}$ associated with the endwall flow is higher up to $z/H \approx 0.05$. On the other hand, the $C_{SKE}$ associated with the PV and TSV displays similar magnitude even though it is lifted off toward the center of the passage. The increase of the $C_{SKE}$ near the endwall results from the increased level of overturning when purge flow is injected. A distinct peak in this region occurs due to the intensified SS corner vortex that has larger spanwise extent. As the PMFR is increased, the peak associated with the PV and TSV is pushed away from the endwall. Comparatively to the NC case, the magnitude of the $C_{SKE}$ associated with this region increases by 154% and 234%, for the increasing PMFR investigated.

*3.5.5 Loss Breakdown.* A loss breakdown is performed to decouple the gross losses computed downstream into inlet BL, profile, and endwall loss. The endwall loss includes the contribution from the endwall BL dissipation and secondary flow mixing. To compute the secondary losses, the profile loss is assumed to be constant along the span:

$$\xi_{end} = \xi_{gross} - \xi_{BL} - \xi_{prof} \tag{9}$$

The gross loss is computed by mass averaging the kinetic energy loss coefficient from Eq. (4) over the measurement area. Opposite to the contours and pitchwise averaged quantities, the purge flow contribution is considered by substituting the freestream total pressure with the mixed-out inlet total pressure. The method reported by de la Rosa Blanco et al. [28], based on a constant-area mixing calculation of the inlet total pressure, is used:

$$P_{0,mix} = \frac{\dot{m}_{main} P_{01,fs} + \dot{m}_{purge} P_{0,cav}}{\dot{m}_{main} + \dot{m}_{purge}} \tag{10}$$

The total pressure inside the splitter is used instead of the $P_0$,cav term. This results in a maximum variation of $P_0$, mix within ±8 Pa for the highest PMFR compared. This variation is not expected to impact the conclusions of the loss breakdown.

The loss breakdown for the investigated cases is displayed in Fig. 15. The gross loss increases when the flat endwall is replaced with the cavity one, and with increasing PMFR in the latter case. The profile loss is similar from case to case as expected since the flow at midspan is not impacted by the purge and secondary flows. The slightly lower loss for the NC is due to the slightly higher outlet Mach number when the blade tests were performed (L5HP measurements were performed on different days). By accounting for the momentum deficit of the inlet BL, it can be concluded that the secondary losses increased with the introduction of the cavity endwall. From the pitchwise distributions, this is justified by the increase in the PV strength (higher flow underturning and $C_{SKE}$ near endwall). The introduction of the purge flow further

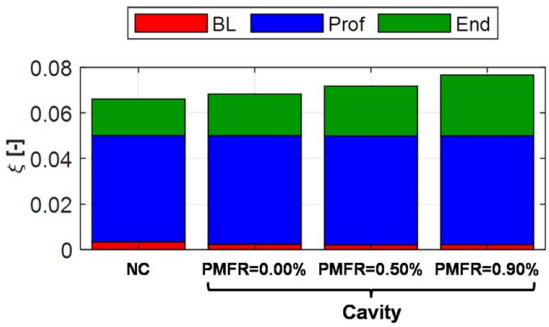


**Fig. 15 Loss breakdown of investigated cases**

**Table 5 Summary of loss contributions for all cases**

| | | Cavity with PMFR | | |
|---|---|---|---|---|
| $\xi$ | NC | 0.00% | 0.50% | 0.90% |
| BL | 0.0034 | 0.0024 | 0.0021 | 0.0022 |
| Prof | 0.0466 | 0.0476 | 0.0477 | 0.0477 |
| End | 0.016 | 0.0183 | 0.0219 | 0.0267 |
| Gross | 0.066 | 0.0682 | 0.0718 | 0.0766 |
| $C_{SKE}$ | 0.0014 | 0.0015 | 0.0034 | 0.0046 |

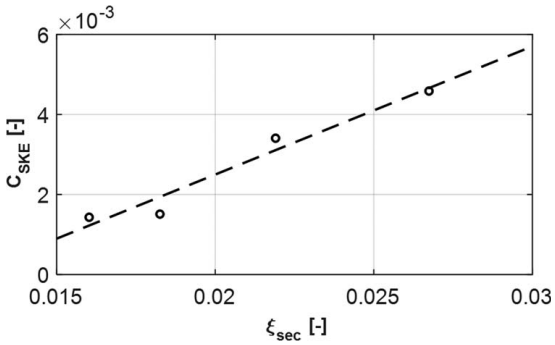


**Fig. 16 Relationship between endwall loss and $C_{SKE}$**

increases the endwall loss. This was expected since the extent of the secondary flow structures along their strength increased with PMFR.

The contribution of all loss components for the cases investigated is displayed in Table 5. The introduction of the cavity endwall alone promotes an increase in the endwall loss by 14% compared to the NC case. The purge flow has the impact of further increasing the secondary losses of lowest PMFR case by 37% with respect to the flat endwall. The highest PMFR case promoted an increase of the secondary losses by 67%. Table 5 also shows the planewise mass averaged $C_{SKE}$ for completeness. The $C_{SKE}$ displays a similar behavior as the endwall loss from case to case.

Figure 16 displays the $C_{SKE}$ in function of the secondary losses. The increase of the $C_{SKE}$ with the endwall loss is represented by a linear trend for the cases investigated in this work. Even though more experimental and/or numerical data would be required to complement the analysis, this result reinforces that the $C_{SKE}$ is linked to the secondary loss generation in linear cascades as highlighted in Refs. [46–48]. This parameter has the added benefit that no loss breakdown was required and that the interpretation of the pitchwise averaged profile was not by the a priori knowledge of the inlet BL profile (overshoots near the endwall in the case of the kinetic energy loss coefficient).

## 4 Conclusions

The steady aerodynamics of a high-speed linear cascade under the presence of unsteady wakes and cavity purge flow were investigated. The cascade was operated at engine-representative Mach and Reynolds numbers, velocity triangles, and purge mass flow ratio. The purpose was to investigate the impact of the cavity geometry and increasing purge flowrate on the aerodynamics of the cascade. The investigation was performed with four different cases: flat endwall, cavity endwall with PMFR = 0.00%, and cavity endwall with PMFR = 0.50% and 0.90%.

Introducing the cavity geometry did not produce meaningful effects on the blade loading near the endwall with exception of the local increase in the isentropic Mach number near the TE. A reduction of the isentropic Mach number by as much as 8% between the LE and velocity peak was found when purge flow impinged on the blade. In the PV location, the isentropic Mach number increased by at least 3% near the velocity peak.

Even though the location and extent of the secondary flow structures was not majorly modified by replacing the flat endwall with the cavity endwall, the increasing PMFR displaced the PV and TSV away from the endwall. The mass-averaged analysis allowed to conclude that the loss associated with the TSV can increase as much as 27% and 40% for the cases of PMFR = 0.50% and 0.90%, respectively, with respect to the flat endwall case. A large region of overturning near the endwall, which was induced by the PV, resulted in a large increase of the $C_{SKE}$ near the endwall when purge flow is injected resultant from the intensified PV. The $C_{SKE}$ associated with the interaction of the PV and TSV remained constant as the cavity endwall was introduced, and it increased by 154% and 234% for the increasing PMFR, relative to the flat endwall case.

The endwall loss was decoupled from the gross loss. It was found that the introduction of the cavity geometry alone promoted an increase of the endwall loss by 14% compared with the flat endwall. The endwall loss increased with the PMFR. An increase of 66% was detected for the case of PMFR = 0.90% when compared to the flat endwall.

The $C_{SKE}$ displayed good robustness in the interpretation of the pitchwise and planewise averaged losses. In the case of the pitchwise losses, this parameter provided a good indication of the presence and interaction of the secondary flow structures downstream without being impacted by the inlet BL (like the kinetic energy loss coefficient). In the overall loss breakdown, it was found that the increase in endwall loss and $C_{SKE}$ displayed an almost linear relationship for the cases investigated in this work.


## Acknowledgment

The authors gratefully acknowledge funding of the SPLEEN project by the Clean Sky 2 Joint Undertaking under the European Unions Horizon 2020 research and innovation program under the grant agreement 820883. The work of Gene Bryan on the assembling and commissioning of the purge flow circuit is also acknowledged.


## Conflict of Interest

There are no conflicts of interest.

## Data Availability Statement

The data and information that support the findings of this article are freely available at: 10.5281/zenodo.7264761.

## Nomenclature

$g$ = blade pitch
$i$ = cascade inlet incidence, $\beta - \beta_{met,in}$
$x$ = location along axial chord
$y$ = location along pitch
$z$ = location along span direction
$C$ = airfoil true chord, coefficient
$H$ = cascade span
$M$ = Mach number
$S$ = location along surface length
$U$ = uncertainty
$K_\omega$ = streamwise vorticity coefficient
$S_L$ = surface length
Prof = profile
Re = Reynolds number
BL = boundary layer
CV = suction side corner vortex

C5HP = cobra-shaped five-hole probe
DP = design point
End = endwall
GTF = geared turbofan
HPT = high-pressure turbine
LE = leading edge
L5HP = L-shaped five-hole probe
LPT = low-pressure turbine
PDF = probability density function
PMFR = purge mass flow ratio
PS = pressure side
PV = passage vortex
PV4HP = pneumatic virtual four-hole probe
SFC = specific fuel consumption
SS = suction side
TE = trailing edge
TG = turbulence grid
TSV = trailing shed vortex
WG = wake generator

### Subscripts and Superscripts

2 = plane 02
3 = plane 03
6 = plane 06
ax = axial
corr = corrected
fs = freestream
in = inlet
is = isentropic
met = metallic
MS = midspan
orif = orifice
out = outlet
rand = random
ref = reference
sec = secondary
SKE = secondary kinetic energy
sys = systematic

### Greek Symbols

$\beta$ = primary flow direction, $\arctan(V_{ax}/V_{tan})$
$\zeta$ = stagger angle
$\xi$ = kinetic energy loss coefficient

## References


[1] Kurzke, J., 2009, "Fundamental Differences Between Conventional and Geared Turbofans," Volume 1: Aircraft Engine; Ceramics; Coal, Biomass and Alternative Fuels; Controls, Diagnostics and Instrumentation; Education; Electric Power; Awards and Honors of Turbo Expo: Power for Land, Sea, and Air, Orlando, FL, June 8–12, pp. 145–153.
[2] Hodson, H. P., and Howell, R. J., 2005, "The Role of Transition in High-Lift Low-Pressure Turbines for Aeroengines," Prog. Aerosp. Sci., **41**(6), pp. 419–454.
[3] Torre, D., Garcia-Valdecasas, G., Puente, A., Hernandez, D., and Luque, S., 2022, "Design and Testing of a Multi-Stage Intermediate Pressure Turbine for Future Geared Turbofans," ASME J. Turbomach., **144**(9), p. 091008.
[4] Hourmouziadis, J., 1989, "Aerodynamic Design of Low Pressure Turbines," AGARD Lecture Series 167, von Karman Institute: Rhode-St-Genèse, Belgium.
[5] Giovannini, M., Rubechini, F., Marconcini, M., Arnone, A., and Bertini, F., 2016, "Analysis of a LPT Rotor Blade for a Geared Engine: Part I—Aero-Mechanical Design and Validation," Volume 2B: Turbomachinery of Turbo Expo: Power for Land, Sea, and Air, Seoul, South Korea, June 13–17, p. V02BT38A053.
[6] Malzacher, F. J., Gier, J., and Lippl, F., 2003, "Aerodesign and Testing of an Aeromechanically Highly Loaded LP Turbine," ASME J. Turbomach., **128**(4), pp. 643–649.
[7] Wang, H. P., Olson, S. J., Goldstein, R. J., and Eckert, E. R. G., 1997, "Flow Visualization in a Linear Turbine Cascade of High Performance Turbine Blades," ASME J. Turbomach., **119**(1), pp. 1–8.
[8] Sieverding, C. H., and Van den Bosche, P., 1983, "The Use of Coloured Smoke to Visualize Secondary Flows in a Turbine-Blade Cascade," J. Fluid. Mech., **134**(1), pp. 85–89.
[9] Langston, L., 2001, "Secondary Flows in Axial Turbines—A Review," Ann. N. Y. Acad. Sci., **934**(1), pp. 11–26.
[10] Sharma, O. P., and Butler, T. L., 1987, "Predictions of Endwall Losses and Secondary Flows in Axial Flow Turbine Cascades," ASME J. Turbomach., **109**(2), pp. 229–236.
[11] Behr, T., 2007, "Control of Rotor Tip Leakage and Secondary Flow by Casing Air Injection in Unshrouded Axial Turbines," Ph.D. thesis, ETH, Zurich, Switzerland.
[12] Volino, R. J., Galvin, C. D., and Ibrahim, M. B., 2013,, "Effects of Periodic Unsteadiness on Secondary Flows in High Pressure Turbine Passages," Volume 6C: Turbomachinery of Turbo Expo: Power for Land, Sea, and Air, San Antonio, TX, June 3–7, p. V06CT42A042.
[13] Ciorciari, R., Kirik, I., and Niehuis, R., 2014, "Effects of Unsteady Wakes on the Secondary Flows in the Linear T106 Turbine Cascade," ASME J. Turbomach., **136**(9), p. 091010.
[14] Satta, F., Simoni, D., Ubaldi, M., Zunino, P., and Bertini, F., 2012, "Profile and Secondary Flow Losses in a High-Lift Lpt Blade Cascade at Different Reynolds Numbers Under Steady and Unsteady Inflow Conditions," J. Thermal Sci., **21**(6), pp. 483–491.
[15] Infantino, D., Satta, F., Simoni, D., Ubaldi, M., Zunino, P., and Bertini, F., 2015, "Phase-Locked Investigation of Secondary Flows Perturbed by Passing Wakes in a High-Lift LPT Turbine Cascade," Volume 2C: Turbomachinery of Turbo Expo: Power for Land, Sea, and Air, Montreal, Quebec, Canada, June 15–19, p. V02CT44A008..
[16] Denton, J. D., 1993, "The 1993 IGTI Scholar Lecture: Loss Mechanisms in Turbomachines," ASME J. Turbomach., **115**, pp. 621–656.
[17] Hunter, S. D., and Manwaring, S. R., 2000, "Endwall Cavity Flow Effects on Gaspath Aerodynamics in an Axial Flow Turbine: Part I—Experimental and Numerical Investigation," Volume 1: Aircraft Engine; Marine; Turbomachinery; Microturbines and Small Turbomachinery of Turbo Expo: Power for Land, Sea, and Air, Munich, Germany, May 8–11, p. V001T03A111.
[18] Gier, J., Stubert, B., Brouillet, B., and de Vito, L., 2003, "Interaction of Shroud Leakage Flow and Main Flow in a Three-Stage LP Turbine," ASME J. Turbomach., **127**(4), pp. 649–658.
[19] Schlienger, J., Pfau, A., Kalfas, A. I., and Abhari, R. S., 2003, "Effects of Labyrinth Seal Variation on Multistage Axial Turbine Flow," Volume 6: Turbo Expo 2003, Parts A and B of Turbo Expo: Power for Land, Sea, and Air, Atlanta, GA, June 16–19, pp. 173–185.
[20] Bohn, D., 1977, "Untersuchung zweier verschiedener axialer Überschallverdichterstufen unter besonderer Berücksichtigung der Wechselwirkungen zwischen Lauf- und Leitrad," RWTH Aachen, Aachen, Germany.
[21] McLean, C., Camci, C., and Glezer, B., 2001, "Mainstream Aerodynamic Effects Due to Wheelspace Coolant Injection in a High-Pressure Turbine Stage: Part I—Aerodynamic Measurements in the Stationary Frame," ASME J. Turbomach., **123**(4), pp. 687–696.
[22] Schrewe, S., Werschnik, H., and Schiffer, H.-P., 2013, "Experimental Analysis of the Interaction Between Rim Seal and Main Annulus Flow in a Low Pressure Two Stage Axial Turbine," ASME J. Turbomach., **135**(5), p. 051003.
[23] Schuepbach, P., Abhari, R. S., Rose, M. G., and Gier, J., 2010, "Influence of Rim Seal Purge Flow on the Performance of an Endwall-Profiled Axial Turbine," ASME J. Turbomach., **133**(2), p. 021011.
[24] Schuepbach, P., Abhari, R. S., Rose, M. G., Germain, T., Raab, I., and Gier, J., 2010, "Effects of Suction and Injection Purge-Flow on the Secondary Flow Structures of a High-Work Turbine," ASME J. Turbomach., **132**(2), p. 021021.
[25] Schreiner, B. D. J., Wilson, M., Li, Y. S., and Sangan, C. M., 2020, "Effect of Purge on the Secondary Flow-Field of a Gas Turbine Blade-Row," ASME J. Turbomach., **142**(10), p. 101006.
[26] Paniagua, G., Denos, R., and Almeida, S., 2004, "Effect of the Hub Endwall Cavity Flow on the Flow-Field of a Transonic High-Pressure Turbine," ASME J. Turbomach., **126**(4), pp. 578–586.
[27] Barigozzi, G., Franchini, G., Perdichizzi, A., Maritano, M., and Abram, R., 2013, "Purge Flow and Interface Gap Geometry Influence on the Aero-Thermal Performance of a Rotor Blade Cascade," Inter. J. Heat Fluid Flow, **44**, pp. 563–575.
[28] de la Rosa Blanco, E., Hodson, H. P., and Vazquez, R., 2008, "Effect of the Leakage Flows and the Upstream Platform Geometry on the Endwall Flows of a Turbine Cascade," ASME J. Turbomach., **131**(1), p. 011004.
[29] Popovic, I., and Hodson, H. P., 2013, "The Effects of a Parametric Variation of the Rim Seal Geometry on the Interaction Between Hub Leakage and Mainstream Flows in HP Turbines," ASME J. Eng. Gas Turbines Power, **135**(11), p. 112501.
[30] Cherry, D., Wadia, A., Beacock, R., Subramanian, M., and Vitt, P., 2005, "Analytical Investigation of a Low Pressure Turbine With and Without Flowpath Endwall Gaps, Seals and Clearance Features," Volume 6: Turbo Expo 2005, Parts A and B of Turbo Expo: Power for Land, Sea, and Air, Reno, NV, June 6–9, pp. 1099–1105..
[31] MacIsaac, G. D., Sjolander, S. A., Praisner, T. J., Grover, E. A., and Jurek, R., 2013, "Effects of Simplified Platform Overlap and Cavity Geometry on the Endwall Flow: Measurements and Computations in a Low-Speed Linear Turbine Cascade," Volume 6A: Turbomachinery of Turbo Expo: Power for Land, Sea, and Air, San Antonio, TX, June 3–7, p. V06AT36A035.
[32] Lopes, G., Simonassi, L., Torre, A. F. M., Patinios, M., and Lavagnoli, S., 2022,, "An Experimental Test Case for Transonic Low-Pressure Turbines—Part 2: Cascade Aerodynamics at On- and Off-Design Reynolds and Mach Numbers," Volume 10B: Turbomachinery—Axial Flow Turbine Aerodynamics;

Deposition, Erosion, Fouling, and Icing; Radial Turbomachinery Aerodynamics of Turbo Expo: Power for Land, Sea, and Air, Rotterdam, Netherlands, June 13–17, p. V10BT30A027.
[33] Lopes, G., Simonassi, L., and Lavagnoli, S., 2022, "Impact of Unsteady Wakes on the Secondary Flows of a High-Speed Low-Pressure Turbine Cascade," Int. J. Turbomach. Propuls. Power, **8**.
[34] Simonassi, L., Lopes, G., and Lavagnoli, S., 2022, "Effects of Periodic Incoming Wakes on the Aerodynamics of a High-Speed Low-Pressure Turbine Cascade," Int. J. Turbomach. Propuls. Power, **8**.
[35] Lavagnoli, S., Lopes, G., Simonassi, L., and Torre, A. F. M., 2023, SPLEEN—High Speed Turbine Cascade – Test Case Database, Zenodo, Switzerland.
[36] Simonassi, L., Lopes, G., Gendebien, S., Torre, A. F. M., Patinios, M., Lavagnoli, S., Zeller, N., and Pintat, L., 2022, "An Experimental Test Case for Transonic Low-Pressure Turbines—Part I: Rig Design, Instrumentation and Experimental Methodology," Volume 10B: Turbomachinery—Axial Flow Turbine Aerodynamics; Deposition, Erosion, Fouling, and Icing; Radial Turbomachinery Aerodynamics of Turbo Expo: Power for Land, Sea, and Air, Rotterdam, Netherlands, June 13–17, p. V10BT30A012.
[37] Pfeil, H., Herbst, R., and Schroder, T., 1983, "Investigation of the Laminar-Turbulent Transition of Boundary Layers Disturbed by Wakes," J. Eng. Power., **105**(1), pp. 130–137.
[38] ASME, 2004, *Measurement of Fluid Flow in Pipes Using Orifice, Nozzle, and Venturi*, The American Society of Mechanical Engineers, New York City.
[39] Barigozzi, G., Franchini, G., Perdichizzi, A., Maritano, M., and Abram, R., 2013, "Influence of Purge Flow Injection Angle on the Aerothermal Performance of a Rotor Blade Cascade," ASME J. Turbomach., **136**(4), p. 041012.
[40] Lenherr, C., Kalfas, A. I., and Abhari, R. S., 2010, "High Temperature Fast Response Aerodynamic Probe," ASME J. Eng. Gas. Turbines. Power., **133**(1), p. 011603.
[41] Bosdas, I., Mansour, M., Kalfas, A. I., Abhari, R. S., and Senoo, S., 2015, "Unsteady Wet Steam Flow Field Measurements in the Last Stage of Low Pressure Steam Turbine," ASME J. Eng. Gas. Turbines. Power., **138**(3), p. 032601.
[42] Abernethy, R. B., Benedict, R. P., and Dowdell, R. B., 1985, "ASME Measurement Uncertainty," ASME J. Fluids Eng., **107**(2), pp. 161–164.
[43] Coleman, H. W., and Steele, W. G., 2018, *Experimentation, Validation, and Uncertainty Analysis for Engineers*, John Wiley & Sons, Hoboken, NJ.
[44] Brown, L. E., 1972, "Axial Flow Compressor and Turbine Loss Coefficients: A Comparison of Several Parameters," J. Eng. Power, **94**(3), pp. 193–201.
[45] Gregory-Smith, D. G., Graves, C. P., and Walsh, J. A., 1988, "Growth of Secondary Losses and Vorticity in an Axial Turbine Cascade," ASME J. Turbomach., **110**(1), pp. 1–8.
[46] Coull, J. D., 2017, "Endwall Loss in Turbine Cascades," ASME J. Turbomach., **139**(8), p. 081004.
[47] Coull, J., Clark, C., and Vazquez, R., 2019, "The Sensitivity of Turbine Cascade Endwall Loss to Inlet Boundary Layer Thickness," J. Global Power Propulsion Soc., **3**, pp. 540–554.
[48] Coull, J. D., and Clark, C. J., 2022, "The Effect of Inlet Conditions on Turbine Endwall Loss," ASME J. Turbomach., **144**(10), p. 101011.
[49] Kacker, S. C., and Okapuu, U., 1982, "A Mean Line Prediction Method for Axial Flow Turbine Efficiency," J. Eng. Power, **104**(1), pp. 111–119.